Supplementary Information for

Increasing certainty in projected local extreme precipitation change

Chao Li[1, 2]*, Jieyu Liu[3], Fujun Du[1, 2], Francis W. Zwiers[4, 5], and Guolin Feng[6, 7]

[1]Key Laboratory of Geographic Information Science, Ministry of Education, East China Normal University, Shanghai, China.

[2]School of Geographic Sciences, East China Normal University, Shanghai, China.

[3]College of Atmospheric Sciences, Lanzhou University, Lanzhou, China.

[4]Pacific Climate Impacts Consortium, University of Victoria, Victoria, British Columbia, Canada.

[5]Key Laboratory of Meteorological Disaster, Ministry of Education, Joint International Research Laboratory of Climate and Environment Change, Nanjing University of Information Science and Technology, Nanjing, China.

[6]School of Physical Science and Technology, Yangzhou University, Yangzhou, China.

[7]Laboratory for Climate Studies, National Climate Center, China Meteorological Administration, Beijing, China.

*Corresponding author: Chao Li, cli@geo.ecnu.edu.cn

This PDF file includes:

Figs. S1 to S18

Table S1

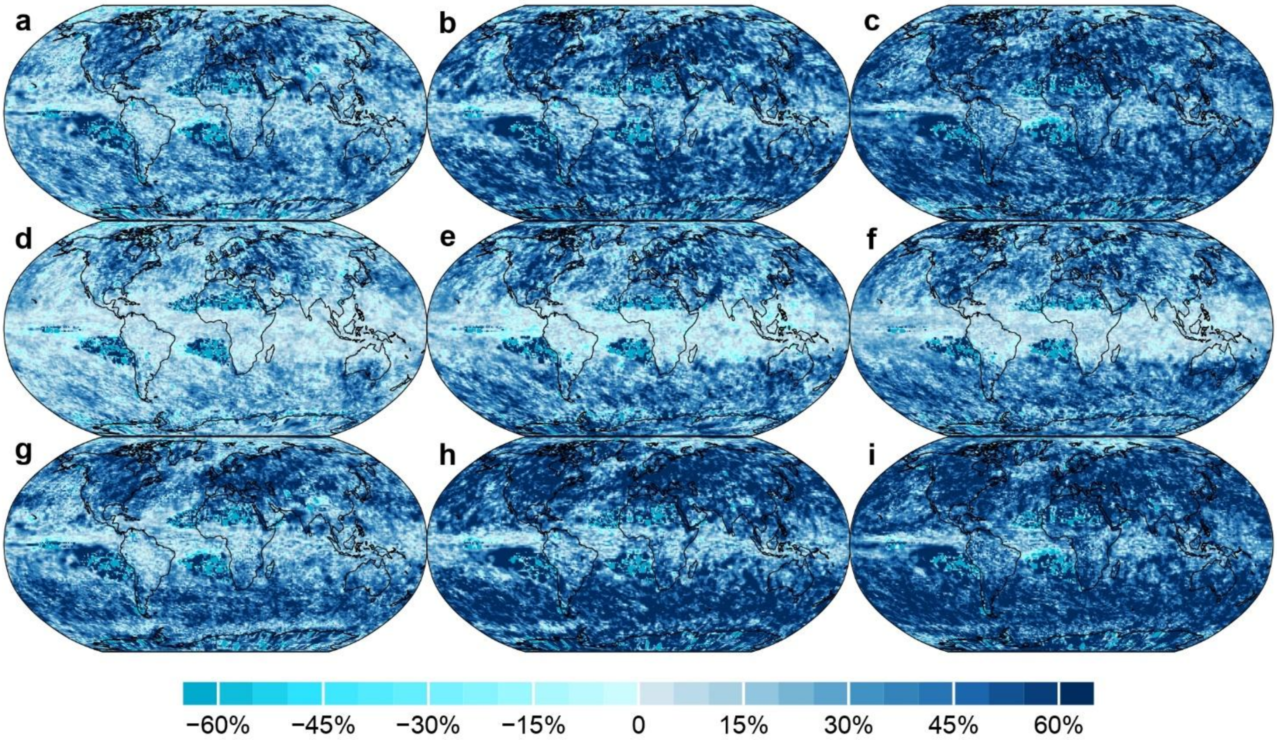

Fig. S1. Internal variability uncertainty reduction by data aggregation. The percentage reductions in the inter-model variances of the diagnosed total (**a**-**c**), thermodynamic (**d**-**f**), and dynamic changes (**g**-**i**) in annual maximum daily precipitation during 2071-2100 relative to 1985-2014 under the SSP5-8.5 (**a**, **d**, and **g**), SSP2-4.5 (**b**, **e**, and **h**), and SSP1-2.6 (**c**, **f**, and **i**) emissions scenarios obtained by spatial and ensemble data aggregation.

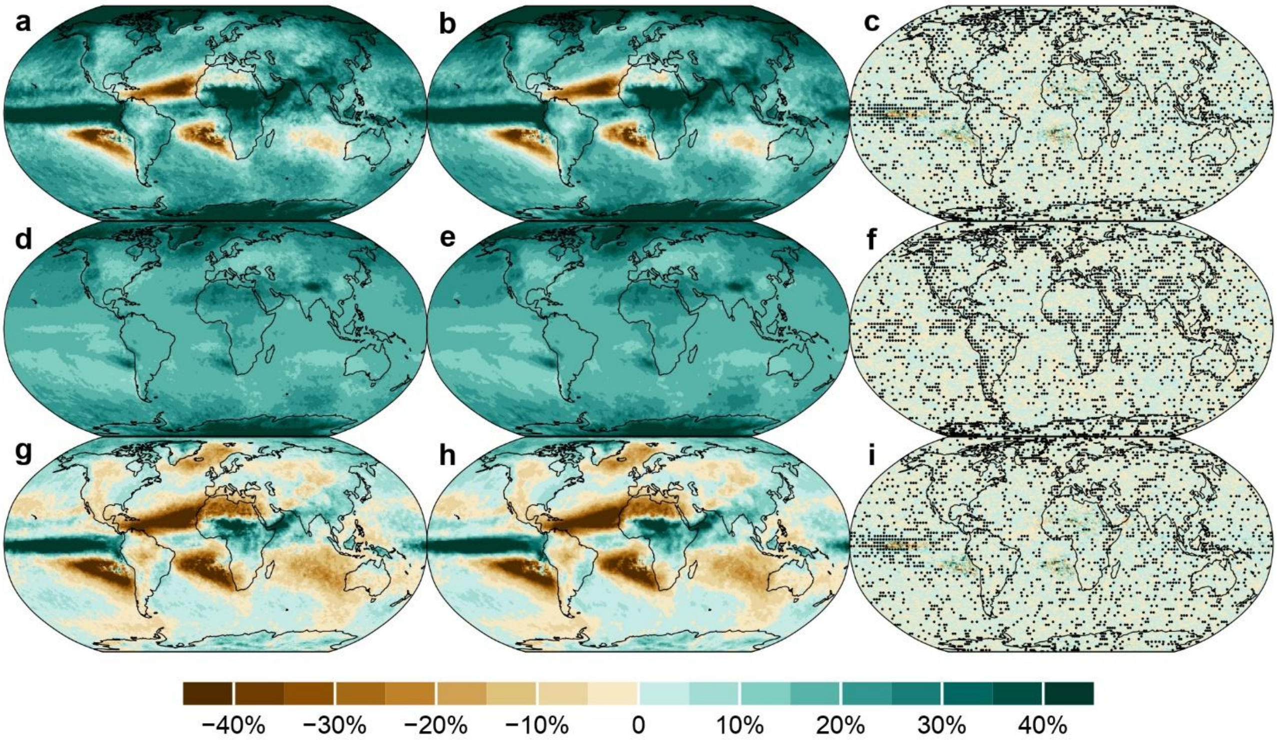

Fig. S2. The effects of spatial data aggregation on estimates of future extreme precipitation changes. The multi-model ensemble medians of the diagnosed total (**a**-**b**), thermodynamic (**d**-**e**), and dynamic changes (**g**-**h**) in annual maximum daily precipitation during 2071-2100 relative to 1985-2014 under the SSP5-8.5 emissions scenarios, derived with ensemble data aggregation alone (**a**, **d**, **g**) and with both ensemble and spatial data aggregation (**b**, **e**, **h**). The effects of spatial aggregation on local extreme precipitation change estimates are shown as the differences in these multi-model ensemble medians (**c**, **f**, and **i**). Stippling marks areas where the changes derived from the two data aggregation strategies are significantly different according to the paired t-test conducted at the 5% level. The fraction of such grid cells is 6.5% for total changes, 7.9% for thermodynamic changes, and 6.1% for dynamic changes.

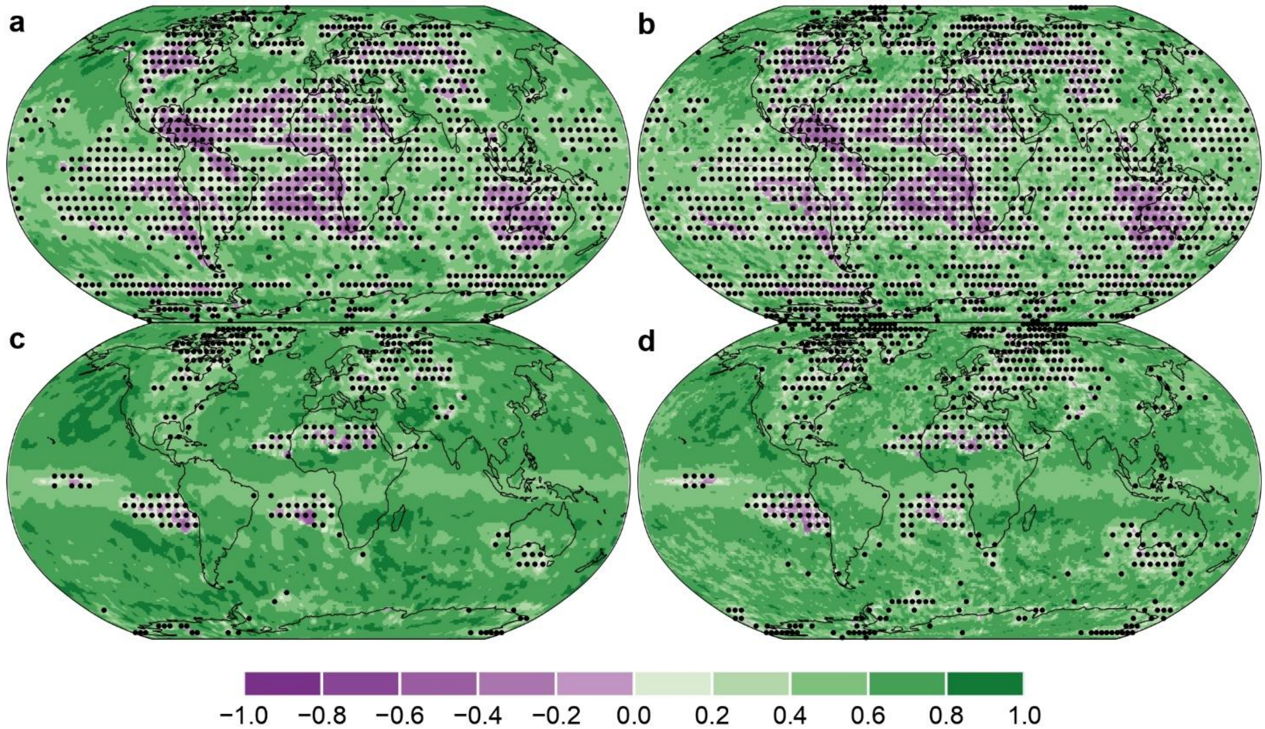

Fig. S3. The effect of data aggregation on emergent constraint relations. The inter-model correlations between the GSAT trends during 1971-2020 and the diagnosed total (**a-b**) and thermodynamic (**c-d**) changes in annual maximum daily precipitation during 2071-2100 relative to 1985-2014 under the SSP5-8.5 emissions scenario estimated with (**a**, **c**) and without (**b**, **d**) spatial and ensemble data aggregation. Stippling marks correlations that are not statistically significant at the 5% level.

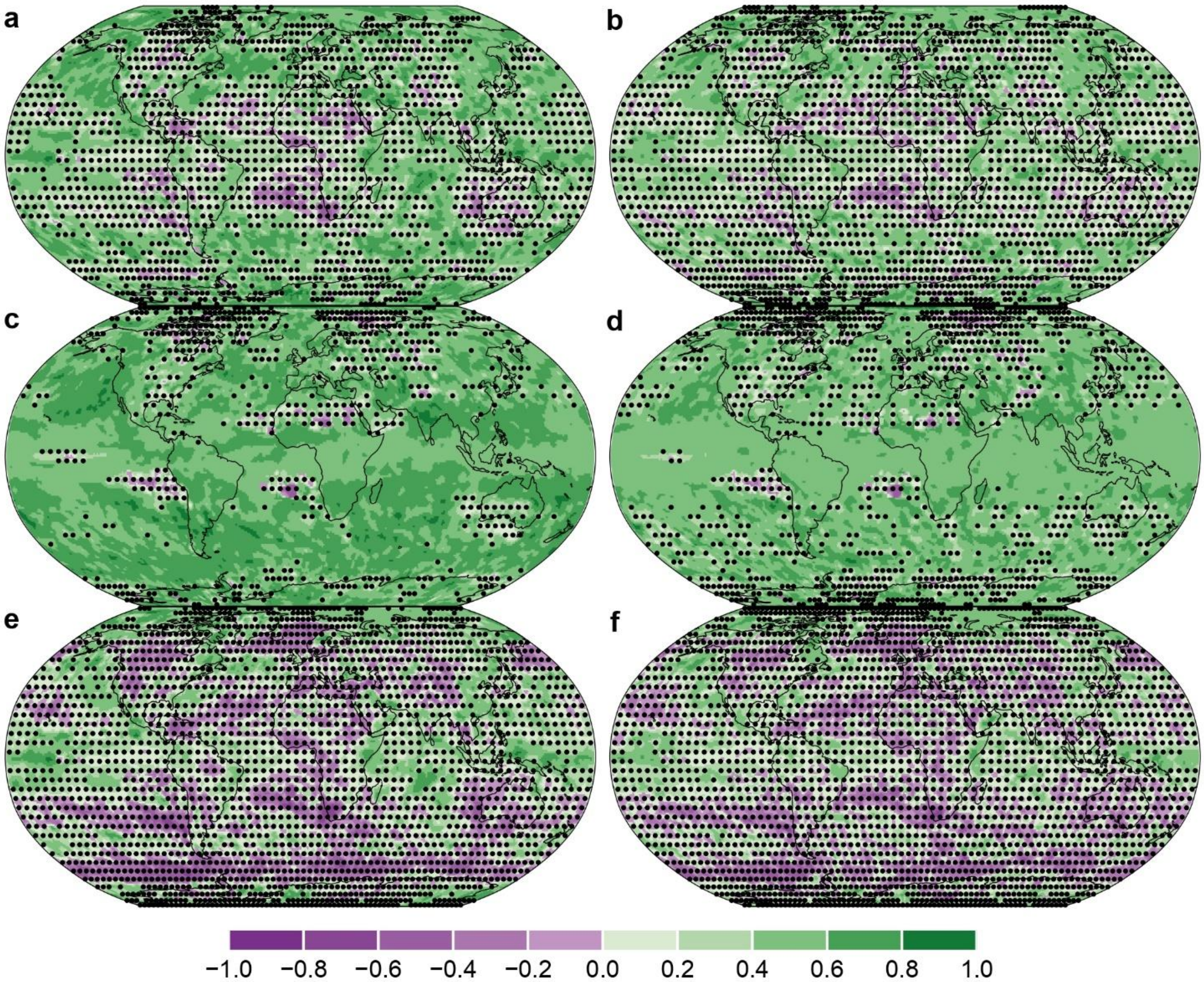

Fig. S4. Correlations between historical warming and future extreme precipitation changes under lower emissions scenarios. As shown in Fig. 3 in the main text, but for the moderate SSP2-4.5 (**a**, **c**, and **e**) and low SSP1-2.6 (**b**, **d**, and **f**) emissions scenarios.

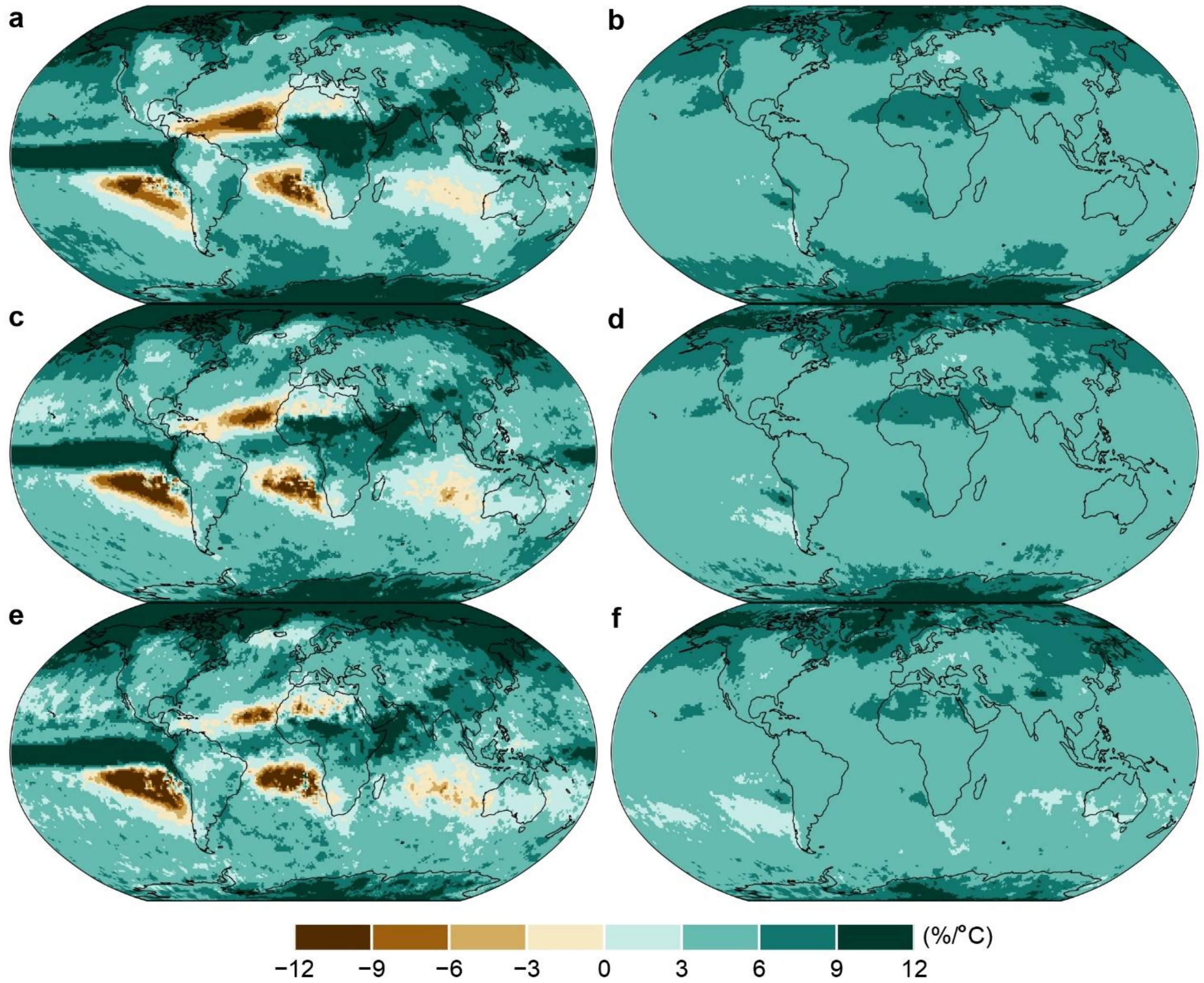

Fig. S5. The projected scaling rates of extreme precipitation changes with global warming. The multi-model median scaling rates of the diagnosed total (**a**, **c**, and **e**) and thermodynamic (**b**, **d**, and **f**) changes in annual maximum daily precipitation during 2071-2100 relative to 1985-2014 with global warming under the SSP5-8.5 (**a**-**b**), SSP2-4.5 (**c**-**d**), and SSP1-2.6 (**e**-**f**) emissions scenarios. The scaling rates do not vary strongly across emissions scenarios, with a few localized exceptions, indicating that the projected annual maximum daily precipitation total and thermodynamic changes depend mainly on the extent of global warming regardless of emissions scenarios.

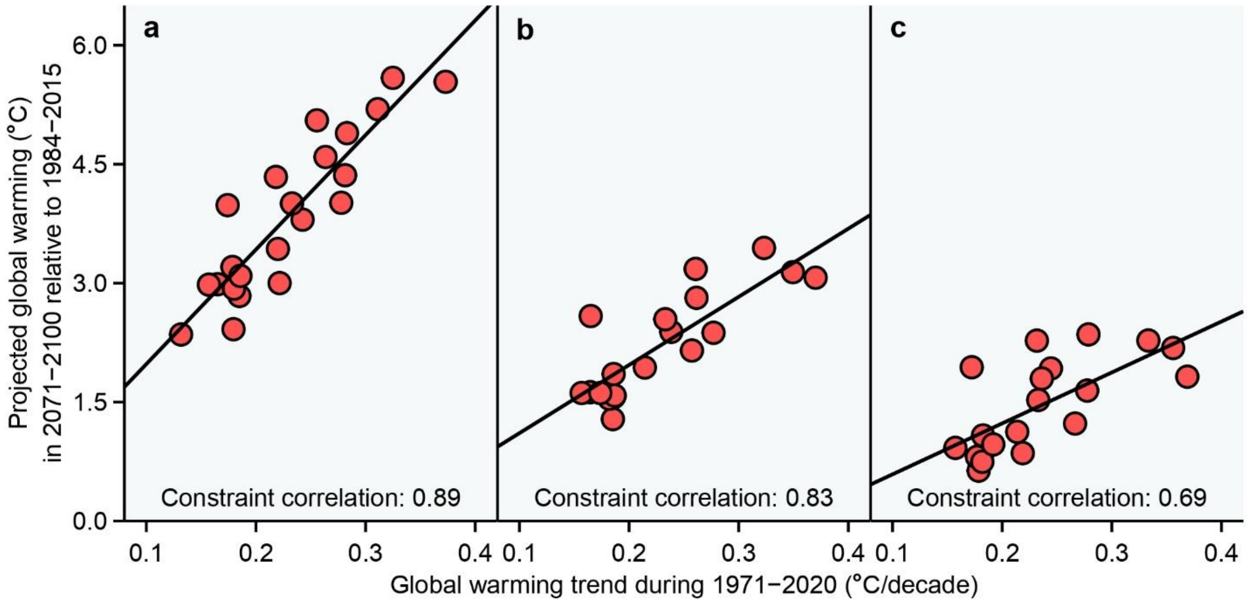

Fig. S6. Scatter plot illustrating the temperature constraint on global warming projections. The scatter points display GSAT changes in 2071-2100 relative to 1985-2014 under the SSP5-8.5 (**a**), SSP2-4.5 (**b**), and SSP1-2.6 (**c**) emissions scenarios versus the 1971–2020 GSAT trends in the studied CMIP6 models (Table S1). In addition to the relatively larger influence of internal climate variability, the reduced constraint correlation under the SSP1-2.6 scenario may be due to the stabilization of global mean temperature in the latter half of the century. This challenges the underlying assumption of using the historical warming trend during a period of transient climate response to constrain future warming projections under stabilization scenarios.

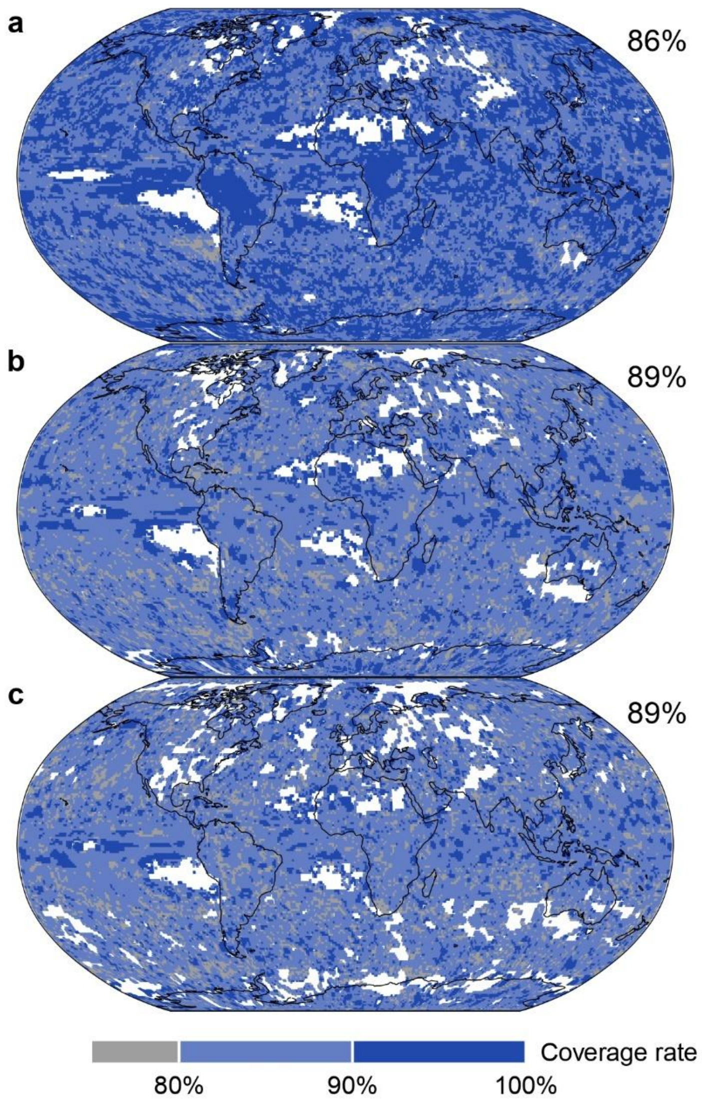

Fig. S7. Out-of-sample validation of the truth coverage rate of the adaptative emergent constraint method. Displayed are the proportions that the pseudo future observations of extreme precipitation changes during 2071-2100 relative to 1985-2014 under the SSP5-8.5 (**a**), SSP2-4.5 (**b**), and SSP1-2.6 (**c**) emissions scenarios fall inside the 90% uncertainty intervals of the projections constrained by the adaptative emergent constraint method, as revealed by a model-based cross-validation (see Methods). The number on the top-right corner show the spatial median coverage rate over the constrained area. Grid cells where the temperature constraint is not applicable in 80% or more of the considered climate models or scaling diagnostic is significantly biased are left blank.

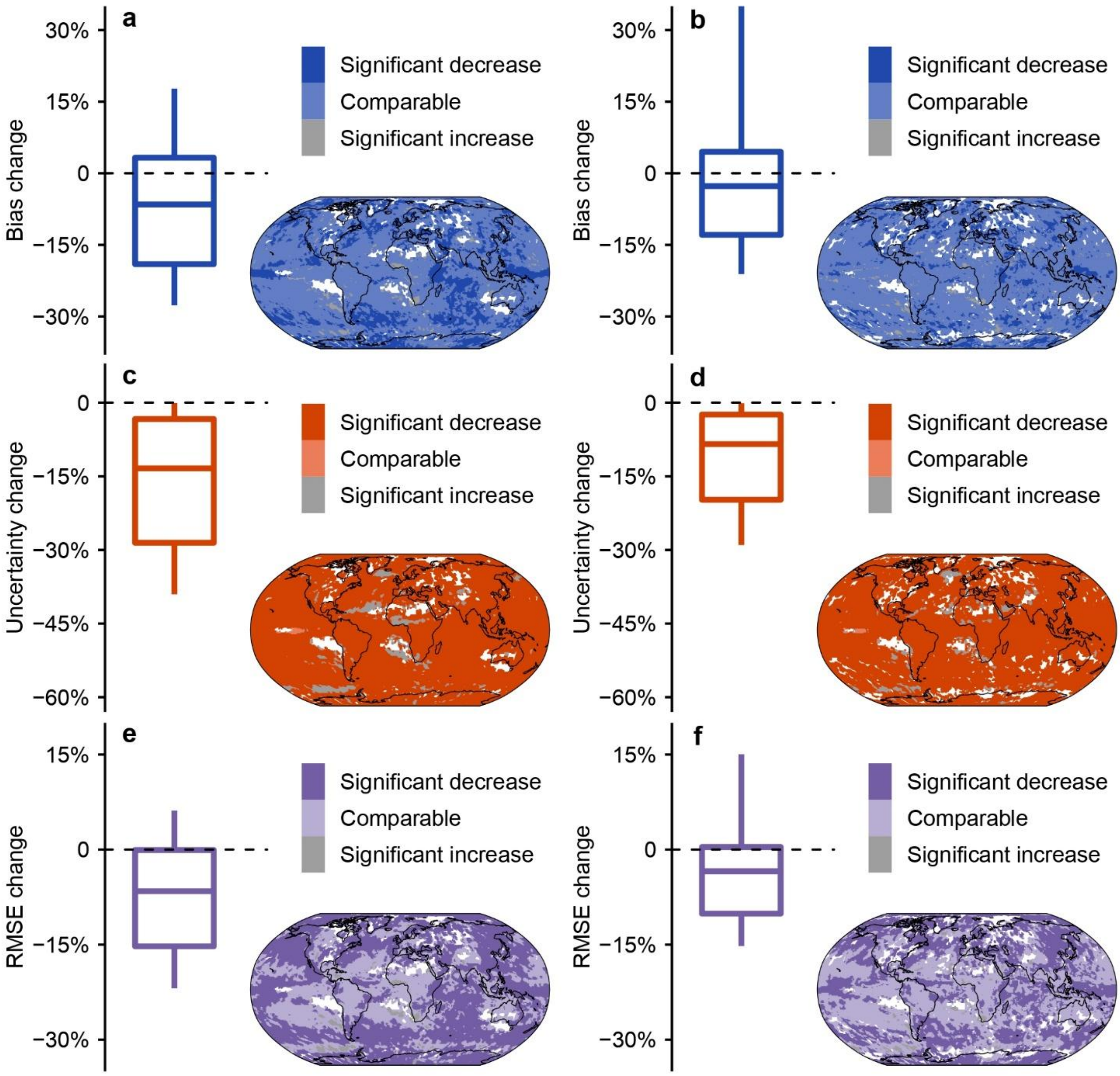

Fig. S8. Out-of-sample validation of the adaptative emergent constraint method for lower emissions scenarios. As shown in Fig. 4 in the main text, but for the moderate SSP2-4.5 (**a**, **c**, and **e**) and low SSP1-2.6 (**b**, **d**, and **f**) emissions scenarios.

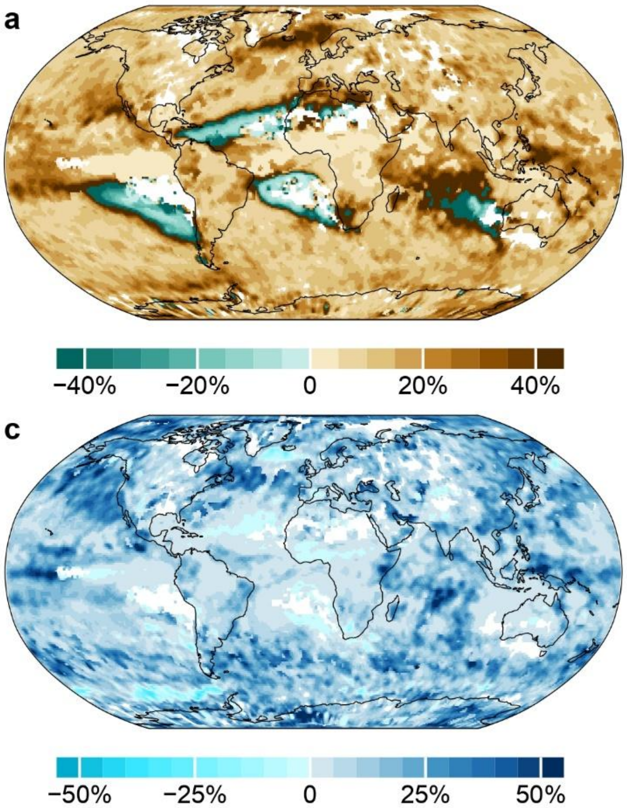

Fig. S9. Comparisons of constrained and unconstrained projections of future extreme precipitation under lower emissions scenarios. As shown in Fig. 5c and 5d in the main text, but for projections under the moderate SSP 2-4.5 (**a** and **c**) and low SSP1-2.6 (**b** and **d**) emissions scenarios.

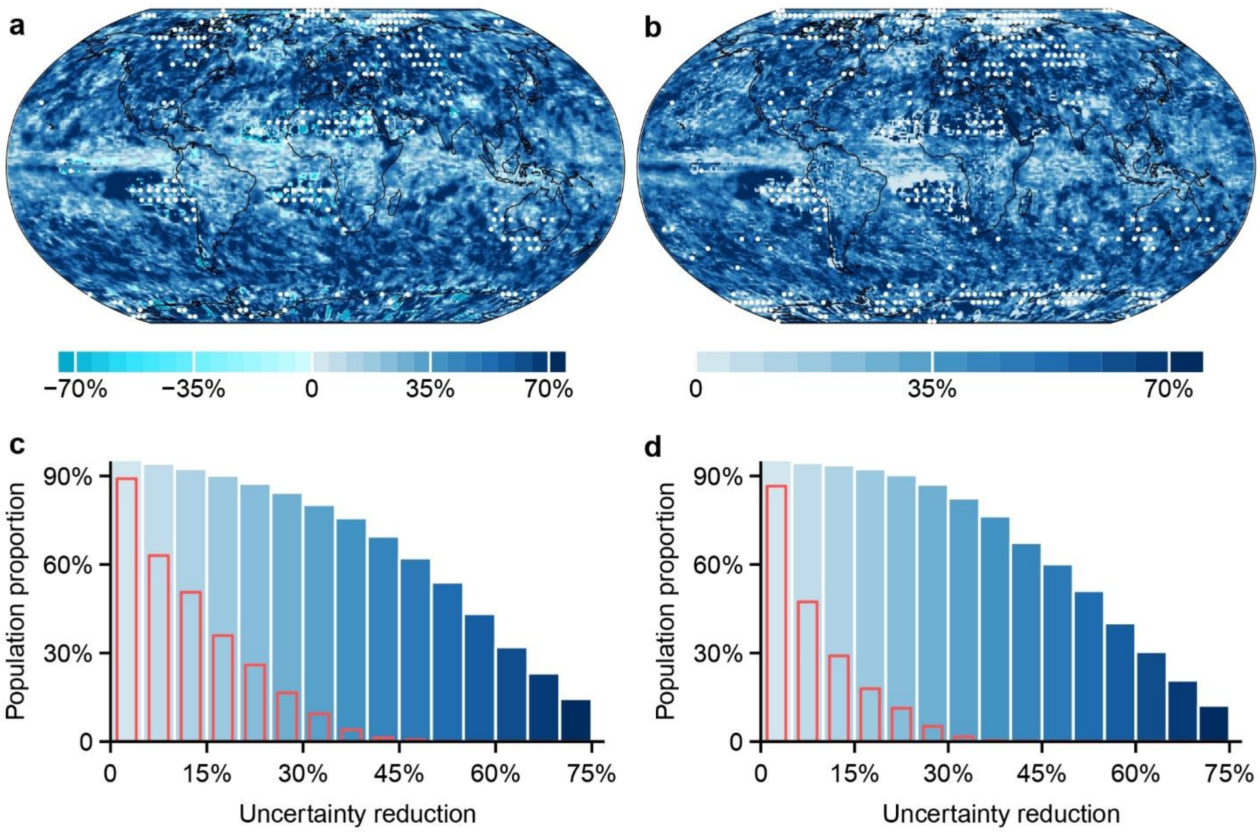

Fig. S10. Total uncertainty reduction in the constrained projections of future extreme precipitation under lower emissions scenarios. As shown in Fig. 6 in the main text, but for projections under the moderate SSP2-4.5 (**a** and **c**) and low SSP1-2.6 (**b** and **d**) emissions scenarios.

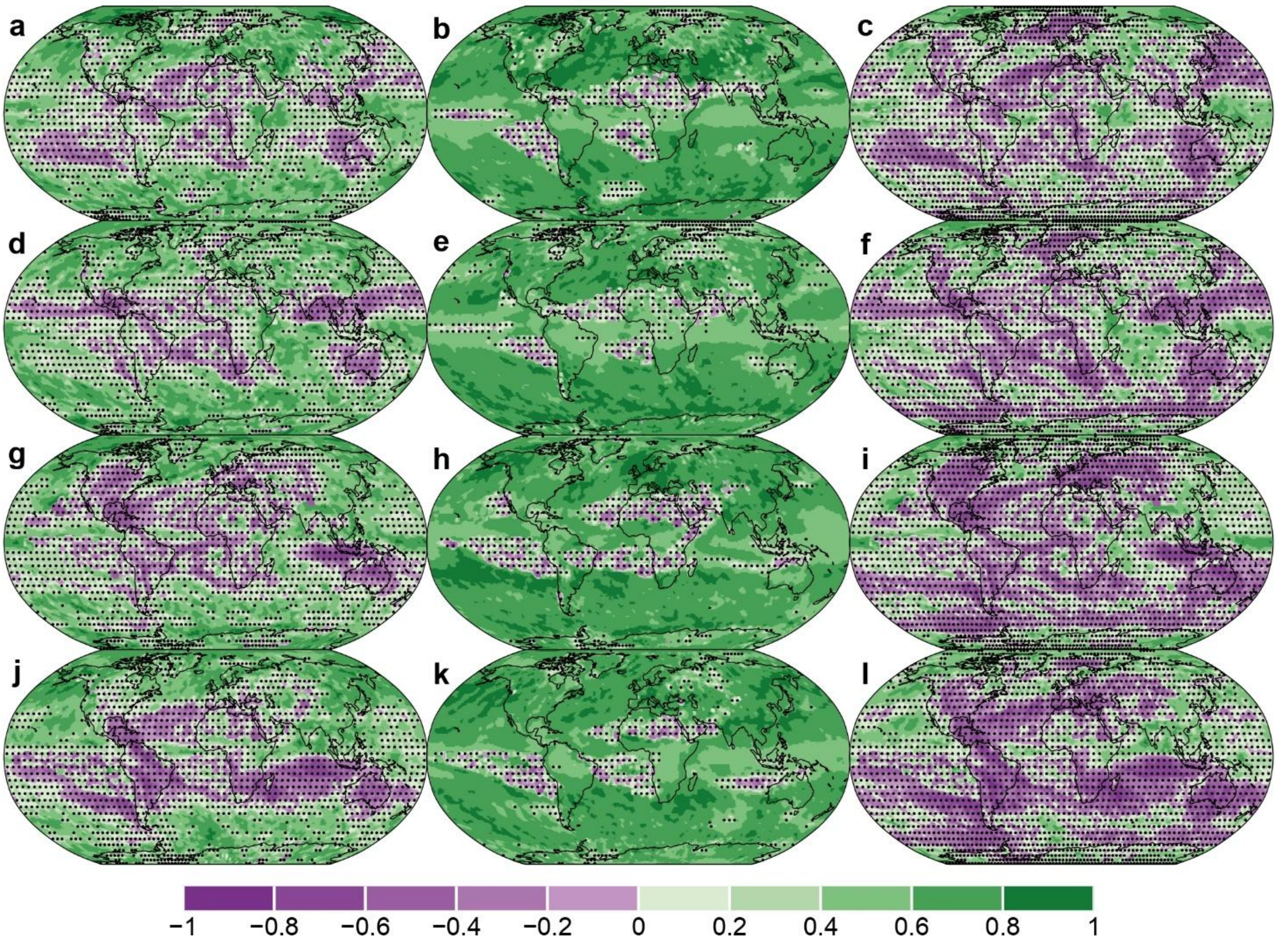

Fig. S11. Correlations between historical warming and future extreme precipitation changes at the seasonal scale. As shown in Fig. 3 in the main text, but for changes in maximum daily precipitation during Dec-Jan-Feb (**a**-**c**), Mar-Apr-May (**d**-**f**), Jun-Jul-Aug (**g**-**i**), and Sep-Oct-Nov (**j**-**k**).

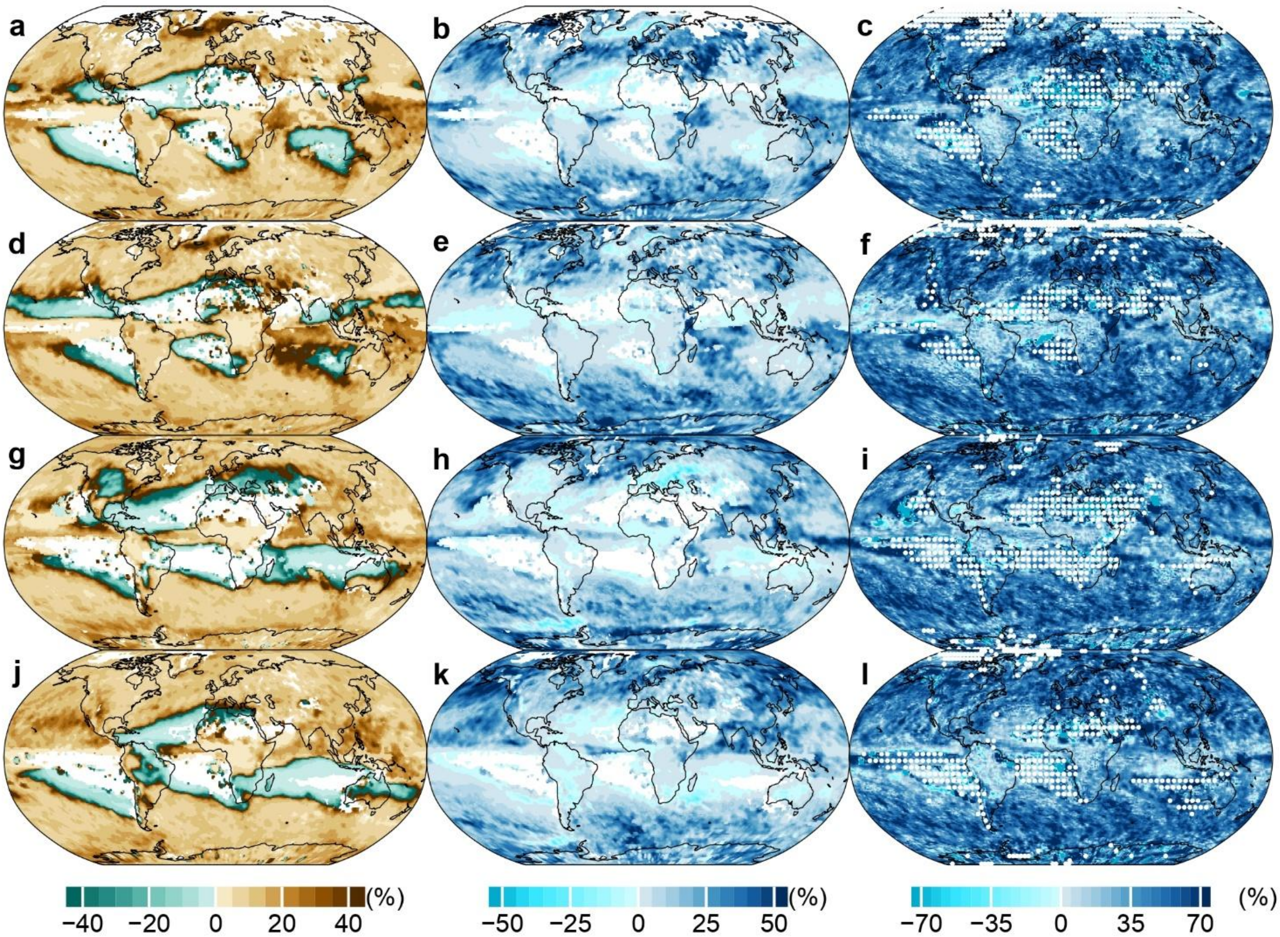

Fig. S12. Comparisons of constrained and unconstrained projections of future extreme precipitation changes at the seasonal scale. Left panels: As shown in Fig. 5c in the main text, but for changes in maximum daily precipitation during Dec-Jan-Feb (**a**), Mar-Apr-May (**d**), Jun-Jul-Aug (**g**), and Sep-Oct-Nov (**j**). Middle and right panels: As shown in Fig. 5d (**b**, **e**, **h**, **k**) and Fig. 6a (**c**, **f**, **i**, **k**) in the main text, but for changes in seasonal extreme precipitation.

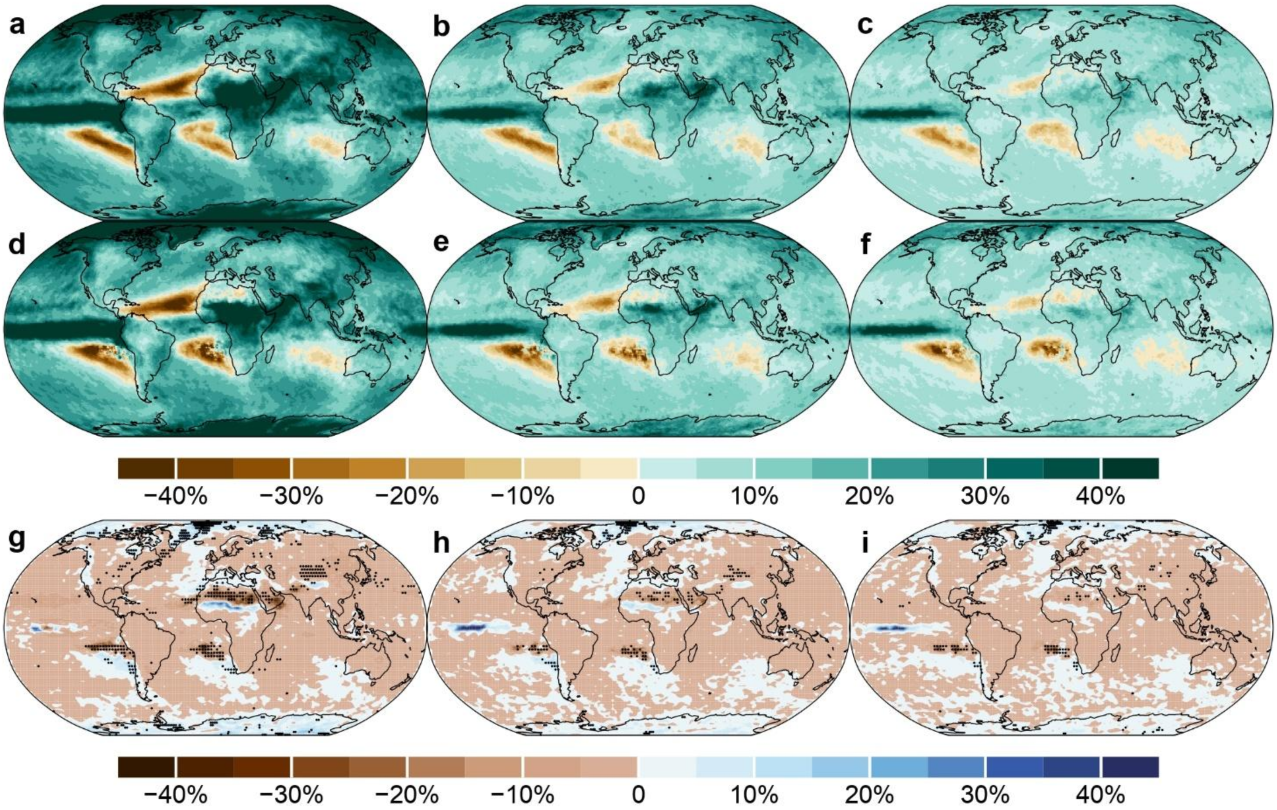

Fig. S13. Evaluation of the physical scaling diagnostic for projections of future extreme precipitation. The multi-model median percentage changes in annual maximum daily precipitation during 2071-2100 relative to 1985-2014 under the high SSP5-8.5 (**a**, **d**, and **g**), moderate SSP2-4.5 (**b**, **e**, and **h**), and low SSP1-2.6 (**c**, **f**, and **i**) emissions scenarios based on model simulated changes (**a-c**) and diagnosed changes (**d-f**) and their differences (**g-i**). Red dots mark grid cells where the diagnosed and model simulated percentage changes are not exchangeable in distribution based on a two-tailed K-S test at the 5% significance level.

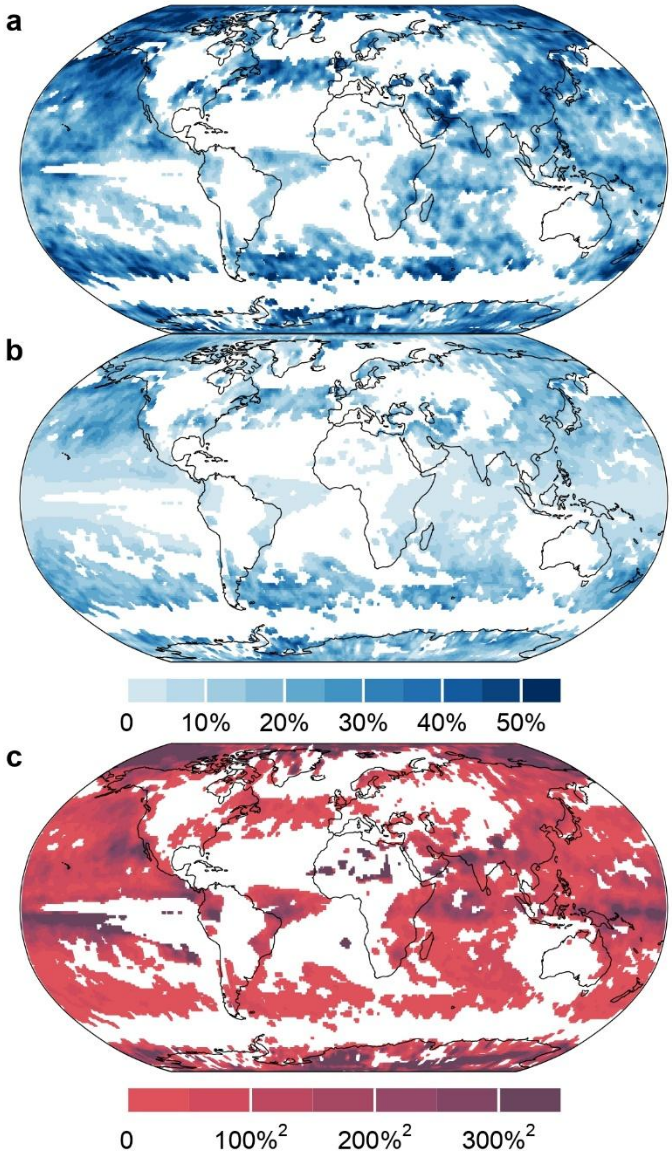

Fig. S14. Enhanced uncertainty reductions in the constrained extreme precipitation changes by positive thermodynamic-dynamic interactions. (**a**) as in Fig. 5D in the main text, but only for grid cells where the inter-model correlation between the thermodynamic and dynamic contributions is positive. (**b**) as in (**a**), but obtained by constraining the thermodynamic change only. (**c**) The inter-model covariances between the thermodynamic and dynamic extreme precipitation changes for grid cells where the covariance is positive.

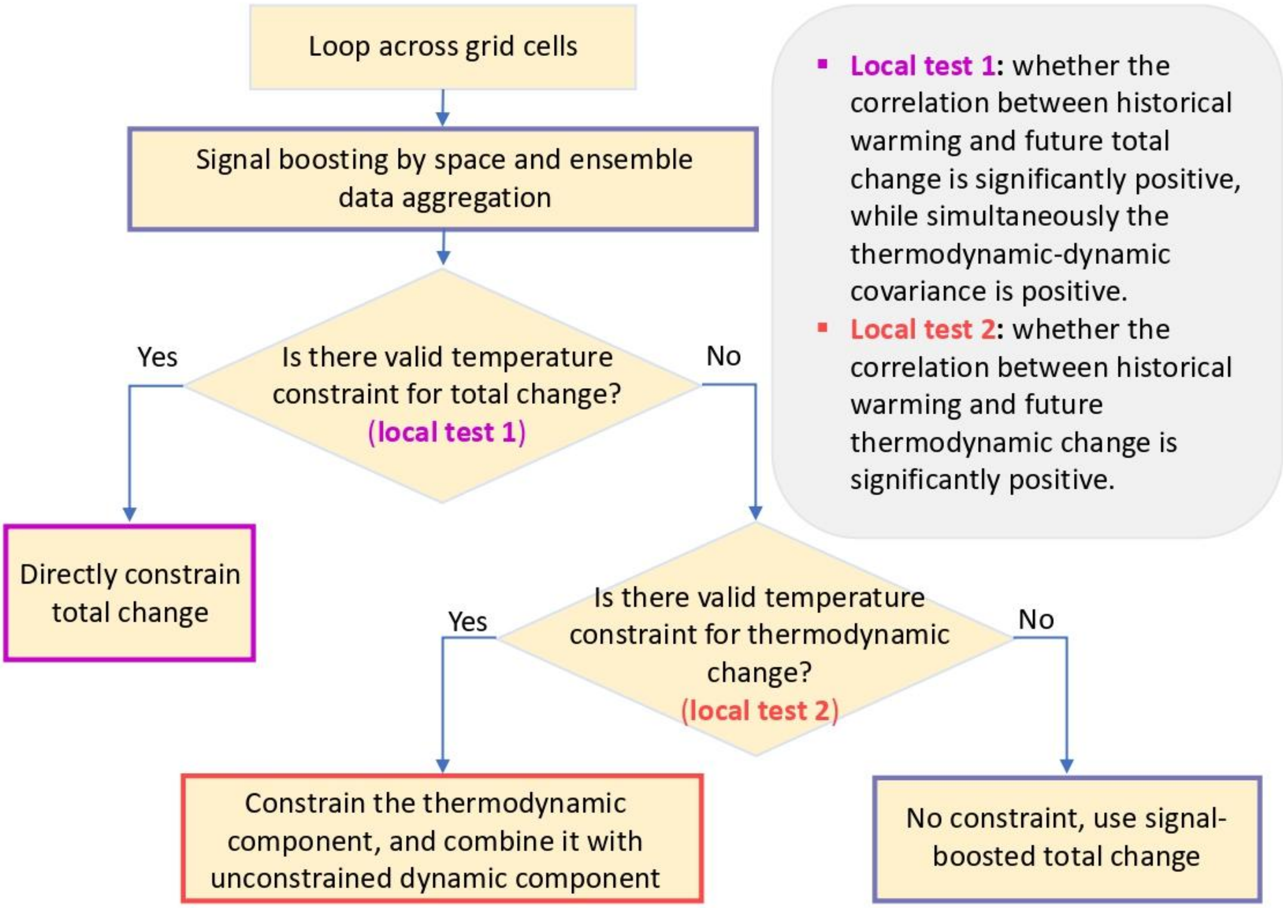

Fig. S15. A schematic diagram illustrating the adaptative constraint method. The method consists of two steps: the first step reduces unforced internal climate variability by aggregating spatial and ensemble simulations; the second step constrains either total or thermodynamic change by a temperature-based constraint, determined by a decision tree that applies two sequential statistical tests. A 10% significance level is used for the statistical tests according to a cross-validation analysis (see Methods).

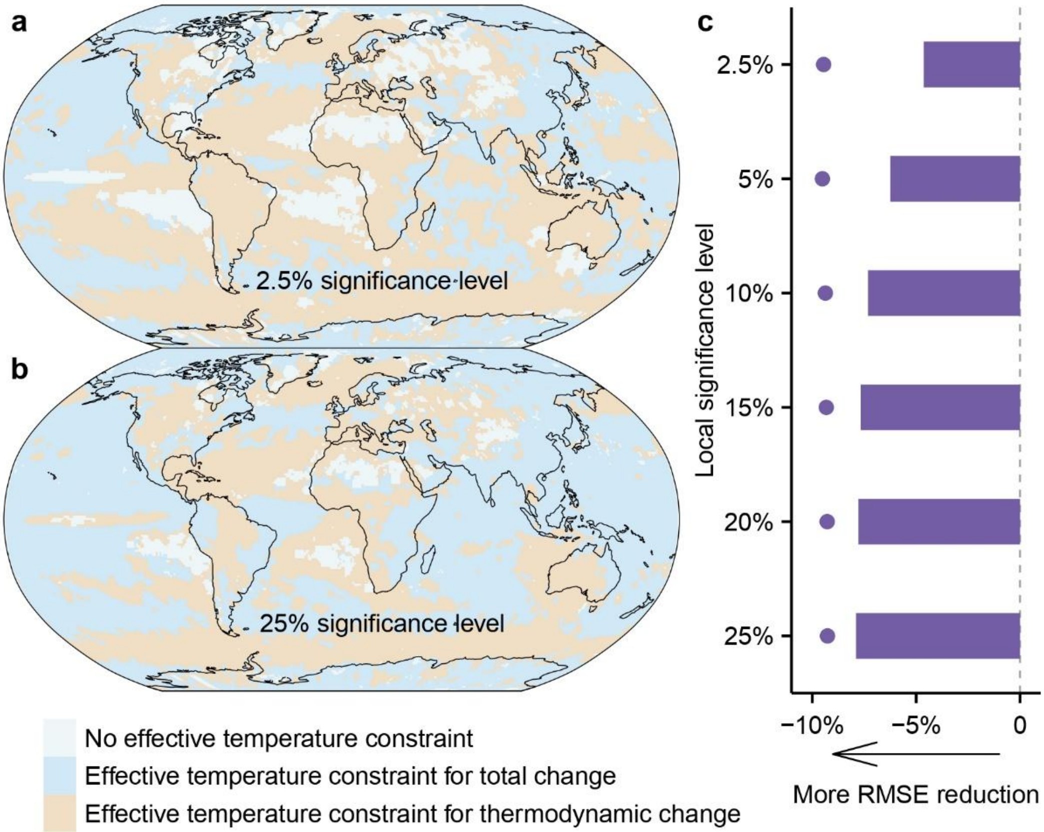

Fig. S16. Optimal configuration analysis for the adaptative constraint method. (**a-b**) The constraint configurations for projected changes in annual maximum daily precipitation during 2071-2100 relative to 1985-2014 under the SSP5-8.5 scenario obtained using significance levels of 2.5% (**a**) and 25% (**b**) for statistical testing in the adaptative constraint method. (**c**) The global mean (bars) and median (points) percentage differences in root mean squared error between constrained and unconstrained changes in annual maximum daily precipitation during 2071-2100 relative to 1985-2014 under the SSP5-8.5 scenario, as revealed by model-based cross-validation with significance levels ranging from 2.5% to 25% for constraint configuration determination.

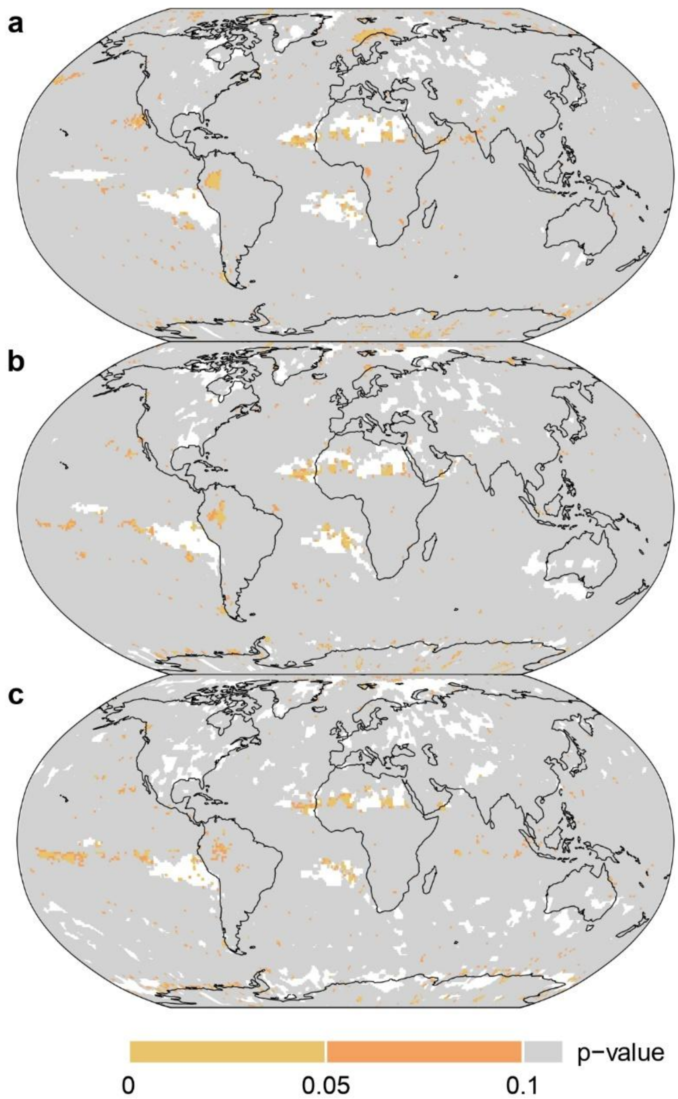

Fig. S17. Evaluation of the validity of the Gaussian assumption for future extreme precipitation projections. Displayed are the p-values of a K-S test assessing whether the diagnosed total or thermodynamic changes in annual maximum daily precipitation during 2071-2100 relative to 1985-2014 follow a Gaussian distribution under the high SSP5-8.5 (**a**), moderate SSP2-4.5 (**b**), and low SSP1-2.6 (**c**) emissions scenarios. The K-S test was applied to the diagnosed total changes at grid cells where valid emergent constraint relationships for total change exist, and to the diagnosed thermodynamic changes at grid cells where valid constraint relationships exist for thermodynamic change only. Grid cells where the temperature constraint is not applicable are left blank.

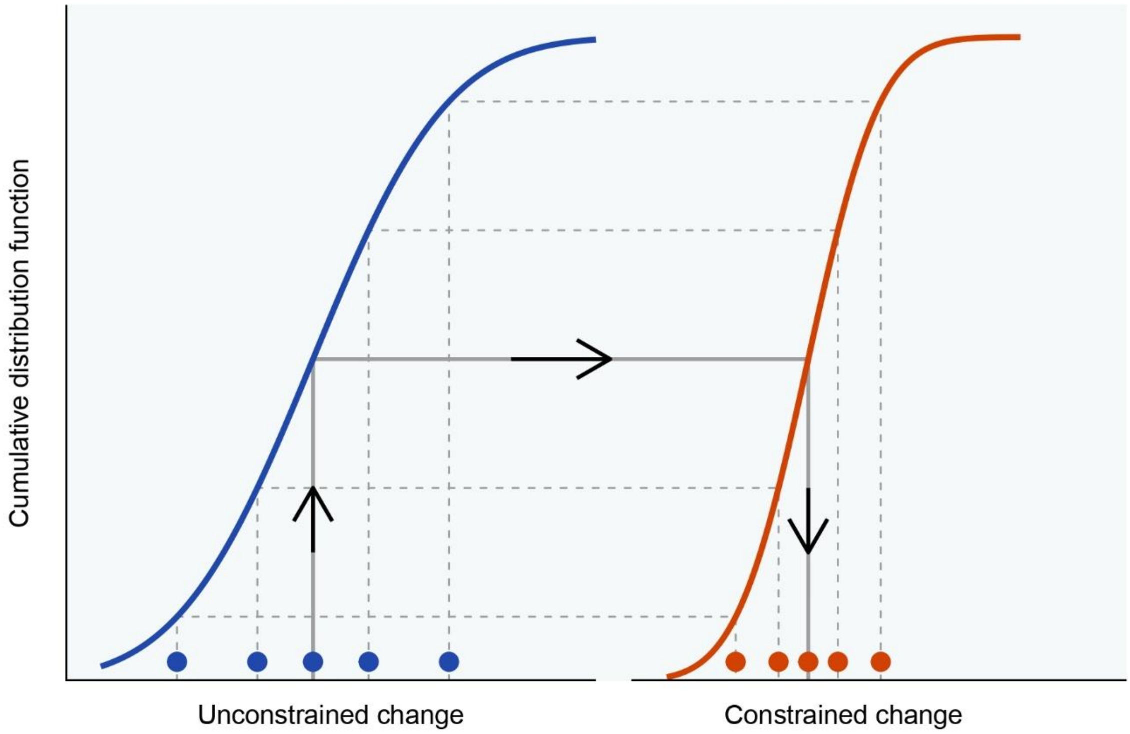

Fig. S18. A schematic illustration of the quantile mapping method. The method maps the unconstrained thermodynamic changes from individual climate models (blue points in the left panel) to the quantiles of the constrained distribution (i.e., the constrained thermodynamic changes; orange points in the right panel) based on the probabilities of the corresponding unconstrained changes in the unconstrained distribution.

Table S1. The analyzed climate models and simulation members with necessary output required by the physical scaling diagnostic for extreme precipitation.

Model	SSP5-8.5	SSP2-4.5	SSP1-2.6
ACCESS-CM2	3	3	3
ACCESS-ESM1-5	40	40	40
CAMS-CSM1-0	1	0	0
CanESM5	20	20	20
CESM2	1	0	0
CESM2-WACCM	3	3	1
CMCC-CM2-SR5	1	1	1
CMCC-ESM2	1	1	1
FGOALS-g3	3	3	3
HadGEM3-GC31-LL	1	4	1
HadGEM3-GC31-MM	1	0	1
MIROC-ES2H	3	3	1
MIROC-ES2L	10	10	10
MIROC6	2	3	3
MPI-ESM1-2-HR	2	2	2
MPI-ESM1-2-LR	30	30	50
MRI-ESM2-0	4	5	5
NESM3	1	1	1
NorESM2-LM	1	1	1
NorESM2-MM	1	1	1
TaiESM1	1	1	1
UKESM1-0-LL	5	4	8